SPECIAL
DYNAMO/CINDY/AMIE/LASP
COLLECTION

Atmospheric Mixed Layer Convergence from Observed MJO Sea Surface Temperature Anomalies

SIMON P. DE SZOEKE

Oregon State University, Corvallis, Oregon

ERIC D. MALONEY

Colorado State University, Fort Collins, Colorado

(Manuscript received 15 May 2019, in final form 26 September 2019)

ABSTRACT

The Madden–Julian oscillation (MJO) dominates tropical weather on intraseasonal 30–90-day time scales, yet mechanisms for its generation, maintenance, and propagation remain unclear. Although surface moist static energy (MSE) flux is greatest under strong winds in the convective phase, sea surface temperature (SST) warms by ~0.3°C in the clear nonconvective phase of the MJO. Winds converging into the hydrostatic low pressure under warm air over the warm SST increase the vertically integrated MSE. We estimate column-integrated MSE convergence using a model of mixed layer (ML) winds balancing friction, planetary rotation, and hydrostatic pressure gradients. Small (0.3 K) SST anomalies associated with the MJO drive 7 W m^{-2} net column MSE convergence averaged over the equatorial Indian Ocean ahead of MJO deep convection. The MSE convergence is in the right phase to contribute to MJO generation and propagation. It is on the order of the total MSE tendency previously assessed from reanalysis, and greater than surface heat flux anomalies driven by intraseasonal SST fluctuations.

1. Introduction

The Madden–Julian oscillation (MJO; Madden and Julian 1971) is the dominant mode of intraseasonal (10–100 day) variability in the tropical atmosphere. Theories for the physics of the MJO are incomplete at explaining the MJO growth and propagation. Despite the potential for improving subseasonal to seasonal predictions, numerical weather prediction models struggle to simulate the MJO (Gottschalck et al. 2010; Kang and Kim 2010; Wang et al. 2014; Lim et al. 2018). Differences among the models are not easily attributed to individual processes. It is likely that the MJO owes its existence to a mixed summation of weakly unstable modes. In moisture mode theories, small positive feedbacks to the column moist static energy (MSE) budget induced by the responses of radiation (Johnson et al. 2015; Del Genio and Chen 2015) and surface fluxes to convection may be all that is needed to overcome weak atmospheric gross moist stability (Raymond and Fuchs 2009) and grow planetary-scale intraseasonal convective anomalies.

Among many possible positive feedbacks, surface fluxes have been proposed to destabilize the atmosphere to the MJO (Krishnamurti et al. 1988; Maloney and Sobel 2004). An early theory for the MJO proposed wind-induced surface heat exchange as important for MJO destabilization and propagation (Emanuel 1987; Neelin et al. 1987). Forcing an atmospheric model with fluxes due to strong SST anomalies enhances its intraseasonal convection (e.g., Flatau et al. 1997), and atmospheric models coupled to a thermodynamically interactive ocean, whose surface ocean temperature evolves conserving enthalpy, are usually better at simulating the MJO than standalone atmospheric models (DeMott et al. 2016; Woolnough et al. 2000; Stan 2018; Marshall et al. 2008).

SST warms during the MJO suppressed phase (Zhang and McPhaden 1995; Hendon and Glick 1997; Shinoda et al. 1998; de Szoeke et al. 2015), attaining its highest temperature just before the onset of active convection. Wind and clouds associated with the convection quickly

Denotes content that is immediately available upon publication as open access.

Corresponding author: Simon P. de Szoeke, sdeszoek@coas.oregonstate.edu

DOI: 10.1175/JCLI-D-19-0351.1

expunge the warm SST anomaly by decreased downward radiative flux, increased surface turbulent heat flux, and increased and upper ocean mixing (Moum et al. 2014), even when the upper ocean entrains warmer water from the salinity stratified barrier layer during westerly wind bursts (Pujiana et al. 2017). Compared to intraseasonal fluxes diagnosed using the time-mean SST field, intraseasonal SST anomalies shift the intraseasonal turbulent heat flux maximum forward in time by ~2 days, so that it is more in phase with the maximum of column MSE (DeMott et al. 2016).

Here we explore another hypothesis, that warm SST anomalies induce hydrostatic low pressure in the marine atmospheric mixed layer (ML), driving convergence in the ML (Lindzen and Nigam 1987; Stevens et al. 2002; Back and Bretherton 2009). This increases moist static energy (MSE) over warm SST anomalies ahead of convection and assists the eastward propagation of the MJO. Reanalysis composited on outgoing longwave radiation (OLR) space–time filtered to isolate the MJO shows warm anomalies below 850 hPa and convergence below about 925 hPa to the east of the minimum OLR (Kiladis et al. 2005, hereafter K05).

Low-level convergence to the east of convection has been proposed as an important mechanism for the sustenance and eastward propagation of the MJO (Hsu and Li 2012; Wang and Li 1994; Wang et al. 2016). Rydbeck and Jensen (2017) demonstrate that persistent warm SST anomalies associated with downwelling oceanic Rossby waves can help to initiate the MJO in the western Indian Ocean. We evaluate the mass and moisture convergence (and hence MSE convergence) due to MJO composite SST anomalies with the wind field calculated from the diagnostic model of Back and Bretherton (2009, hereafter BB09). Because the mean MSE profile decreases to the middle troposphere then increases to the tropopause, upward vertical velocity in the lower troposphere increases MSE by vertical advection, while upward vertical velocity in the upper troposphere decreases MSE (Back and Bretherton 2006). By mass conservation, convergence in the ML implies vertical velocities in the lower troposphere that increase column MSE.

We estimate convergence due to SST gradients related to the MJO in several steps. Section 2 composites the SST anomalies measured by satellite on the Real-time Multivariate MJO index (RMM; Wheeler and Hendon 2004). Section 3 shows the atmospheric temperature structure correlated to the SST. Section 4 integrates the hydrostatic geopotential, averaged over the depth of the ML, due to the temperature anomalies induced by SST. Section 5 solves for the ML winds and convergence from the geopotential gradients using a version of the BB09 linear model. Multiplying by the ML moisture, section 6 presents the SST-induced moisture convergence, and its effect on the column MSE in each phase of the RMM. Section 7 compares this SST-induced MSE convergence to previous estimates of intraseasonal surface flux anomalies (DeMott et al. 2016) and to intraseasonal MSE advection from the Dynamics of the MJO (DYNAMO) field experiment sounding array (Johnson and Ciesielski 2013).

2. Intraseasonal SST composites

We first estimate intraseasonal SST anomalies associated with the MJO. We use passive microwave SST retrievals that measure SST through clouds, avoiding biases that result from clouds obscuring infrared SST retrievals. To remove the influence of seasonal and interannual variability, we first high-pass filter Tropical Rainfall Measuring Mission (TRMM) Microwave Imager (TMI; Gentemann et al. 2004; Wentz et al. 2015) 25-km gridded swath SST by subtracting the 120-day running mean, iterated three times over the 1998–2013 record.

SST and SST gradient anomalies are assigned to their RMM phase (phases 1–8; Wheeler and Hendon 2004) according to the RMM daily time series. We select data from austral summer (November–April), when the equatorial MJO defined by the RMM is strongest. To better detect the effect of the MJO, we composite only those days when the RMM amplitude is equal to or greater than one standard deviation. To maximize the statistical significance of the composites, MJO events were not subdivided further, such as into primary and successive events (Matthews 2008; Straub 2013). The number of days is between 653 and 797 for every RMM phase. TMI precipitation anomalies are likewise composited by RMM phase.

Most satellite SST data products are composed of nocturnal surface retrievals. At night the upper ocean is not thermally stratified by solar absorption (Gentemann et al. 2003; Clayson and Bogdanoff 2013). SST rises in the intraseasonal convectively suppressed phase in large part because of strong solar diurnal warming and reduced mixing near the ocean surface. Using latitude–longitude gridded TMI swath data that record the time of day of each retrieval, we average daylight and nocturnal means for each RMM phase separately to avoid diurnal aliasing from the sun-asynchronous TRMM satellite orbit. Daylight and nocturnal composites are averaged together with equal weight after the RMM compositing. The results are not sensitive to using either full-day or nocturnal composites, indicating that intraseasonal SST variability is well represented by ocean mixed layer temperature, as sampled by nocturnal SST.

Figure 1 shows the SST composite anomalies and positive precipitation anomalies for each RMM phase.

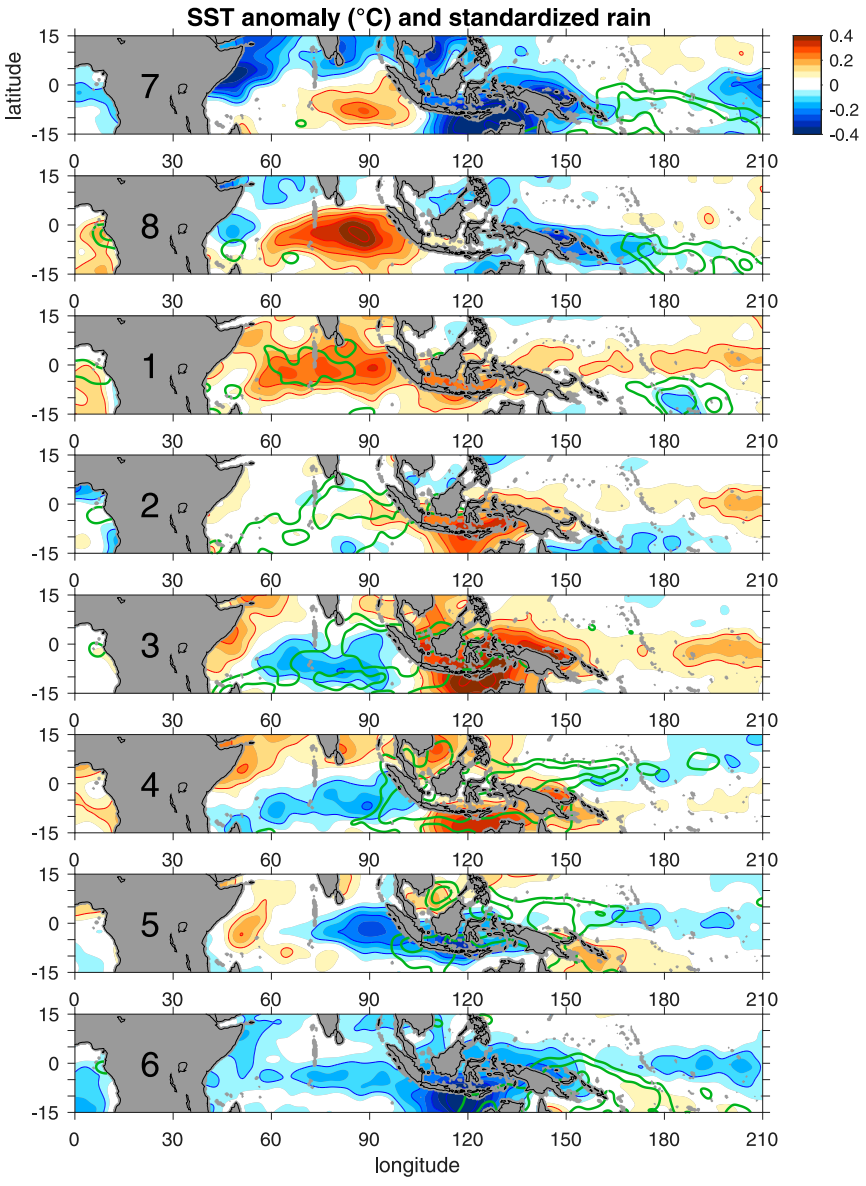

FIG. 1. TMI SST anomaly composites (contour interval 0.05°C) for each phase of the Wheeler and Hendon (2004) RMM index. The number printed over Africa indicates the RMM phase. Positive TMI precipitation anomalies are contoured in units of standard deviations (green).

In the Indian Ocean, where the MJO forms and begins to propagate eastward, the warmest SST anomalies are found to the east of positive precipitation anomalies.

Intraseasonal warm SST anomalies associated with the RMM in November–April propagate northward from the southern ITCZ (5°–10°S) in phase 7 to the equator in phases 8 and 1 (Fig. 1). Cold SST anomalies likewise propagate from the ITCZ to the equator in phases 3–5. This northward SST propagation is consistent with warming the SST beneath the location of the climatological southern ITCZ after convection shifts off the ITCZ and onto the equator in the convective phase of the MJO. The RMM phase 7–8 composites also show a cool band over the northern Indian Ocean in the suppressed phase of the MJO. This may be analogous to the cessation of the northern ITCZ in the October 2011 MJO. Active convection in the ITCZ and suppressed convection on the equator allowed equatorial SST to warm, driving equatorial convergence before the onset of equatorial convection (Moteki 2015).

Eastward propagation along the equator follows the northward propagation. Cold SST anomalies propagate

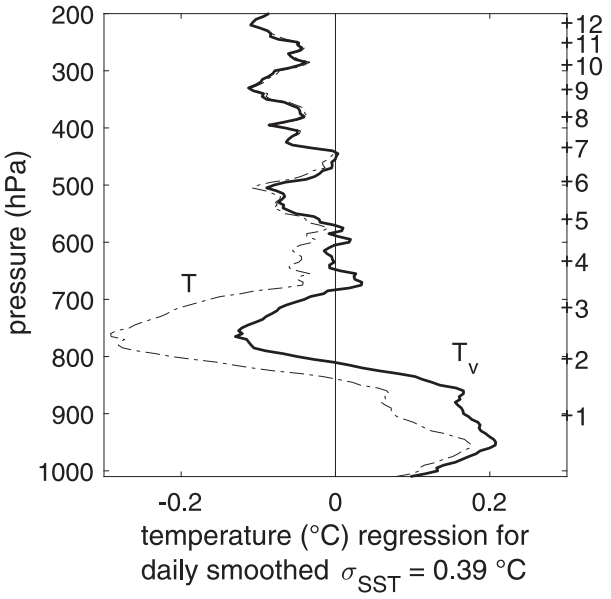

FIG. 2. DYNAMO R/V *Revelle* sounding temperature and virtual temperature projection (°C) onto daily filtered SST anomalies. The standard deviation of the filtered SST is 0.39°C. Vertical height is indicated on the right axis.

zonally along the equator from the central Indian Ocean to the Maritime Continent in phases 3–6. Warm anomalies lead, and cold SST anomalies follow, the MJO convection along its path through the seas between Indonesia and Australia. Warm SST anomalies in phases 2–4 and cold anomalies in phases 6–8 propagate southward from the equator to the South Pacific ITCZ. Large positive SST anomalies also develop in phases 3–4 (and negative anomalies in phases 6–7) in the Maritime Continent between Java and Australia.

3. Atmospheric density structure

In order for the SST to generate pressure anomalies in the ML, it must be related to negative density anomalies in the atmosphere. On 3-times-daily running averaged SST, we regress temperature and virtual temperature anomalies from DYNAMO radiosondes (Yoneyama et al. 2013; Johnson and Ciesielski 2013) released from the R/V *Revelle* in October–November 2011 at the equator, 80°E (Fig. 2). Radiosondes sampled about every 3 h. Virtual temperature anomalies of about 0.2°C, half the strength of daily low-pass-filtered SST anomalies (σ_{SST} = 0.4°C;, Fig. 2) were observed below 850 hPa. The positive temperature regression reaches above the cloud-base height to about 830 hPa (1.5 km), before reversing sign over the rest of the depth of the shallow convection (700 hPa or 3 km).

The signs of these anomalies are consistent with the warmer atmospheric mixed layer in equilibrium with the warmer SST in the suppressed phase, but a relatively cool upper shallow cumulus cloud layer. Water vapor anomalies in the lower atmosphere reinforce the (light) density anomaly due to temperature below 800 hPa, as demonstrated by the projection of virtual temperature on SST. The virtual temperature effect of water vapor on density largely cancels that of cool temperature in the 700–800-hPa layer. Since DYNAMO sampled 2–3 intraseasonal SST cycles and convective events, this projection provides only anecdotal, rather than statistically significant, evidence of the intraseasonal atmospheric temperature response associated with SST. The DYNAMO period exhibited considerable synoptic, mesoscale, and other variability unrelated to intraseasonal SST variability.

An MJO composite of a longer record (from K05, before the DYNAMO experiment) corroborates equatorial temperature anomalies of 0.2°C reach from the surface to 850 hPa, for convection centered over 150°E (Fig. 7 of K05). The DYNAMO and K05 composites have maximum temperature anomalies at 925–850 hPa rather than at the surface. This may due to cold pools, which penetrate the subcloud mixed layer and spread out along the surface in thin layers only ~100 m deep (de Szoeke et al. 2017). The K05 temperature anomaly spans from the eastern edge of the deep convection to the shore of the eastern Pacific Ocean. From the date line to 140°W, the low-level warm anomalies reach 700 hPa, suggesting that shallow convection to the east of the intraseasonal deep convection homogenizes the temperature.[1] Warm anomalies associated with the deep convection would also affect the surface pressure, but in this study we model only the effect of the subcloud mixed layer temperature that is most closely related to SST.

4. Hydrostatic geopotential anomalies

Gradients of geopotential along constant pressure surfaces describe the force on the air in the ML. In this section we integrate the temperature anomalies in the hydrostatic equation to compute the geopotential anomalies averaged over the depth of the ML. We assume the ML temperature $T = T_0 + T_s$ is a constant base state temperature T_0 plus an anomaly T_s that

[1] Our MJO SST anomaly in phase 5 (Fig. 1), when convection is centered on 150°E, does not extend as far eastward across the equatorial Pacific as in the K05 composite. The RMM index we use (Wheeler and Hendon 2004) includes only the leading two eastward co-propagating modes. The filters of K05 retain zonal mean anomalies, including a mode of variability that zonally extends intraseasonal convection eastward in warm El Niño–Southern Oscillation (ENSO) years (Kessler 2001).

is vertically uniform throughout the subcloud mixed layer, to $p_T = 925\,\text{hPa}$ (about $z_T = 780\,\text{m}$). This layer extends slightly above the cumulus cloud base over the tropical warm pool, and corresponds to the warm anomaly east of convection in K05. We disregard variations in temperature and pressure above this (de Szoeke et al. 2015; Johnson and Ciesielski 2013) in accordance with the weak temperature gradient approximation (Sobel et al. 2001). In fact, there are small temperature gradients above the ML associated with synoptic waves and convective cloud heating. The following calculations are linear, so the contribution to the geopotential (and the wind) from the free troposphere and from the ML can be separated and superposed. Here we focus only on the geopotential associated with temperature changes of the ML associated with SST. The geopotential Z hydrostatically integrates the density, $dZ = -RTd\ln p$, downward from $p_T = 925\,\text{hPa}$ to the surface pressure $p_S \approx 1010\,\text{hPa}$, where R is the gas constant:

$$Z(p) = Z_T - R(T_0 + T_s)\ln(p/p_T). \tag{1}$$

Only T_s has a horizontal gradient. The zonal (x) derivative is thus $Z_x(p) = -R\ln(p/p_T)(T_s)_x$.

We assume the 1010–925-hPa ML winds are homogeneously mixed, and average the acceleration from the geopotential gradients over the ML. The mass-weighted geopotential derivative for the subcloud ML is found by vertically averaging the horizontal gradient of (1):

$$\int_{p_T}^{p_S} Z_x dp/(p_S - p_T) = -(T_s)_x R\{p_T + p_S[\ln(p_S/p_T) - 1]\}/(p_S - p_T). \tag{2}$$

The factor relating the acceleration of the ML to the temperature gradient is

$$\gamma \equiv \int_{p_T}^{p_S} Z_x\, dp/[(T_s)_x(p_S - p_T)] = -R\{p_T + p_S[\ln(p_S/p_T) - 1]\}/(p_S - p_T). \tag{3}$$

For $p_T = 925$ and $p_S = 1010\,\text{hPa}$, this factor is $\gamma = -12.8\,\text{m}^2\,\text{s}^{-2}\,\text{K}^{-1}$. For twice the depth, $p_T = 850\,\text{hPa}$, the coefficient is slightly more than doubled, to $\gamma = -25.6\,\text{m}^2\,\text{s}^{-2}\,\text{K}^{-1}$. If the temperature anomaly is T_s at $p_S = 1010\,\text{hPa}$ and decreases proportionally to $\ln p$, to zero at $p_T = 925\,\text{hPa}$, then the coefficient for the average geopotential gradient force coefficient is $\gamma = -4.1\,\text{m}^2\,\text{s}^{-2}\,\text{K}^{-1}$, about 1/3 of the coefficient of acceleration for vertically uniform temperature. In Fig. 2, perhaps due to confounding atmospheric temperature variability unrelated to SST, the virtual temperature anomaly is about half that of SST from the surface to about 800 hPa, which is weaker yet deeper than we assumed to calculate our SST–pressure coefficient γ.

For our choice of $\gamma = -12.8\,\text{m}^2\,\text{s}^{-2}\,\text{K}^{-1}$, a SST gradient of 0.4 K over 12° latitude would accelerate a wind from rest to $1.7\,\text{m}\,\text{s}^{-1}$ in 5 days (~1 MJO phase), were the geopotential acceleration not balanced by friction and Coriolis force. In the next section, we solve for the balanced wind.

5. The SST-induced wind and divergence model

We apply the BB09 ML wind model to the geopotential gradients. The governing equations for the ML zonal u and meridional wind v are

$$u_t = -Z_x - ru + fv, \tag{4}$$

$$v_t = -Z_y - rv - fu, \tag{5}$$

where f is the Coriolis parameter, r is the Rayleigh friction coefficient, and $-(Z_x, Z_y)$ is the layer-average geopotential gradient acceleration. Subscripts indicate partial derivatives.

This model includes entrainment friction at the top of the ML. We assume the wind above the ML is not related to the SST anomalies and linearize the entrainment friction coefficient about the mean wind shear at the top of the inversion. Stevens et al. (2002) found that ML model winds match observations for a $h = 500$-m layer and entrainment velocity of $1\,\text{cm}\,\text{s}^{-1}$, yielding an entrainment Rayleigh drag coefficient of $r_T = w_e/h = 2 \times 10^{-5}\,\text{s}^{-1}$. The entrainment friction is greater than the surface drag $r_S = C_D U/h \approx 1.5 \times 10^{-5}\,\text{s}^{-1}$ with aerodynamic drag coefficient $C_D = 1.3 \times 10^{-3}$ and mean wind speed $U = 6\,\text{m}\,\text{s}^{-1}$. Substituting our mixed layer depth $h = 780\,\text{m}$, corresponding to $p_T = 925\,\text{hPa}$, with these constants, we adopt a ML Rayleigh friction coefficient of

$$r = r_T + r_S = 2.2 \times 10^{-5}\,\text{s}^{-1} \approx 2\,\text{day}^{-1}. \tag{6}$$

For comparison, the Coriolis parameter is $f = 3.8 \times 10^{-5}\,\text{s}^{-1}$ at 15°N. This Rayleigh friction coefficient implies that the winds reach frictional balance within a day, and so are nearly steady on the time scale of intraseasonal SST anomalies.

Following BB09, we model the steady ML wind that balances the pressure gradient, rotation, and drag by zeroing both sides of (4) and (5). The steady velocities are

$$u = -(rZ_x + fZ_y)/(r^2 + f^2), \tag{7}$$

$$v = (fZ_x - rZ_y)/(r^2 + f^2). \tag{8}$$

The horizontal divergence of this wind $\nabla_H \cdot \mathbf{V} = u_x + v_y$ is

$$\nabla_H \cdot \mathbf{V} = -\frac{r}{r^2+f^2}[Z_{xx}+Z_{yy}] + \frac{\beta}{(r^2+f^2)^2}[(r^2-f^2)Z_x + 2frZ_y], \quad (9)$$

where $\beta = f_y$ is the meridional derivative of the Coriolis parameter. The first term with the Laplacian $Z_{xx} + Z_{yy}$ is usually an order of magnitude larger than the second (β) term. Using the Rayleigh friction coefficient $r = 3.5 \times 10^{-5}\,\mathrm{s}^{-1}$ (Stevens et al. 2002; BB09) for a 500-m layer would scale the divergence down by a factor of 0.64. The wind and divergence are completely linear operations, so that convergence over a warm patch of SST is completely symmetric with divergence from a cold patch of SST.

Divergence is calculated from (9) using finite difference approximations for Z_x, Z_y, Z_{xx}, and Z_{yy} on smoothed SST fields for each RMM phase (Fig. 1). Centered finite differences approximate first and second spatial derivatives to at least second-order accuracy using a three-point stencil near data voids at coasts, and up to eighth-order accuracy using a nine-point stencil far from data voids. The spatial gradients amplify high-wavenumber noise in the SST observations. This spatial differentiation procedure uses 3.25° × 3.25° filtered composite SST fields. Its gradients are less noisy than, but not qualitatively different from, those resulting from filtering composite averages of spatial gradients of the sparse gridded daily TMI SST swath observations.

Divergence diagnosed from the SST composite mean for each phase of the RMM (Fig. 1) is shown in Fig. 3. Only divergence composites whose one-sided confidence interval exceeds zero with a probability of at least 0.95 are shaded. The significance level varies with the variance of the SST derivatives and the number of realizations at each location and each phase, but is approximately $3 \times 10^{-7}\,\mathrm{s}^{-1}$ everywhere. (The weakest shaded contour levels in Fig. 3 are $\pm 2 \times 10^{-7}\,\mathrm{s}^{-1}$.) The significance level is estimated for each location and RMM phase from all finite differences of computed from pairs of all neighboring daylight or night SST realizations within 48 h of each other. The median number of these zonal and meridional differences is 380. White noise in the SST retrievals strongly affects the spatial derivatives. The 3.25° × 3.25° (13 × 13 points) spatial filter reduces noise variance by a factor of 3.8×10^{-6} for first derivatives, and 1.1×10^{-7} for second derivatives.

ML convergence accompanies warm SST in the suppressed phase east of the intraseasonal rain maximum from the central Indian Ocean to the far west Pacific in phases 8, 1, 2, and 3. The warm SST and related ML convergence end at the onset of intraseasonal deep convection. Divergence accompanies cool anomalies following and to the west of intraseasonal deep convection. Meridional convergence is responsible for most of the systematic intraseasonal convergence anomalies (not shown) because of zonally elongated intraseasonal SST anomalies with weak zonal gradients.

6. MSE convergence

Vertical advection of dry static energy, $s = c_p T + Z$, is balanced by diabatic heating (mostly net latent heating of condensation) so that the vertical velocity only affects the MSE through moisture advection. Because moisture falls off rapidly with height in the atmosphere, ML convergence pumps moister air from the ML deeper into the atmospheric column, increasing its integrated moist static energy, $h = s + Lq$.

We will show that the ML horizontal convergence is responsible for most of the convergence of moisture due to the SST-induced winds. A secondary part is due to horizontal advection of moisture. Conservation of water is written

$$q_t + \mathbf{u} \cdot \nabla_3 q = 0. \quad (10)$$

The three-dimensional advection $\mathbf{u} \cdot \nabla_3 q$ can be expressed in terms of flux divergence and the specific humidity q times divergence:

$$q_t + \nabla_3 \cdot (\mathbf{u}q) - q(\nabla_3 \cdot \mathbf{u}) = 0, \quad (11)$$

and the divergence $(\nabla_3 \cdot \mathbf{u})$ is zero because the large-scale density structure of the atmosphere is hydrostatic and its flow is incompressible. We express the advection of water vapor alternatively in flux form, and ignore vertical fluxes at the surface and top of the atmosphere. Separating the flux divergence into horizontal and vertical components yields

$$q_t = -\nabla_H \cdot (\mathbf{V}q) - (\omega q)_p. \quad (12)$$

The vertical integral of the (0.25° × 0.25° grid scale) vertical flux divergence $(\omega q)_p$ is zero over the whole atmosphere, so

$$-g^{-1}\int_{p_S}^{0} q_t\, dp = -g^{-1}\int_{p_S}^{0} -\nabla_H \cdot (\mathbf{V}q)\, dp. \quad (13)$$

Having eliminated the vertical flux, we expand the horizontal flux divergence into divergence and advection components:

$$-g^{-1}\int_{p_S}^{0} q_t\, dp = g^{-1}\int_{p_S}^{0} [q(\nabla_H \cdot \mathbf{V}) + \mathbf{V} \cdot \nabla_H q]\, dp. \quad (14)$$

Convergence of mass in the ML is balanced by divergence aloft, yet little *moisture* diverges aloft. To estimate

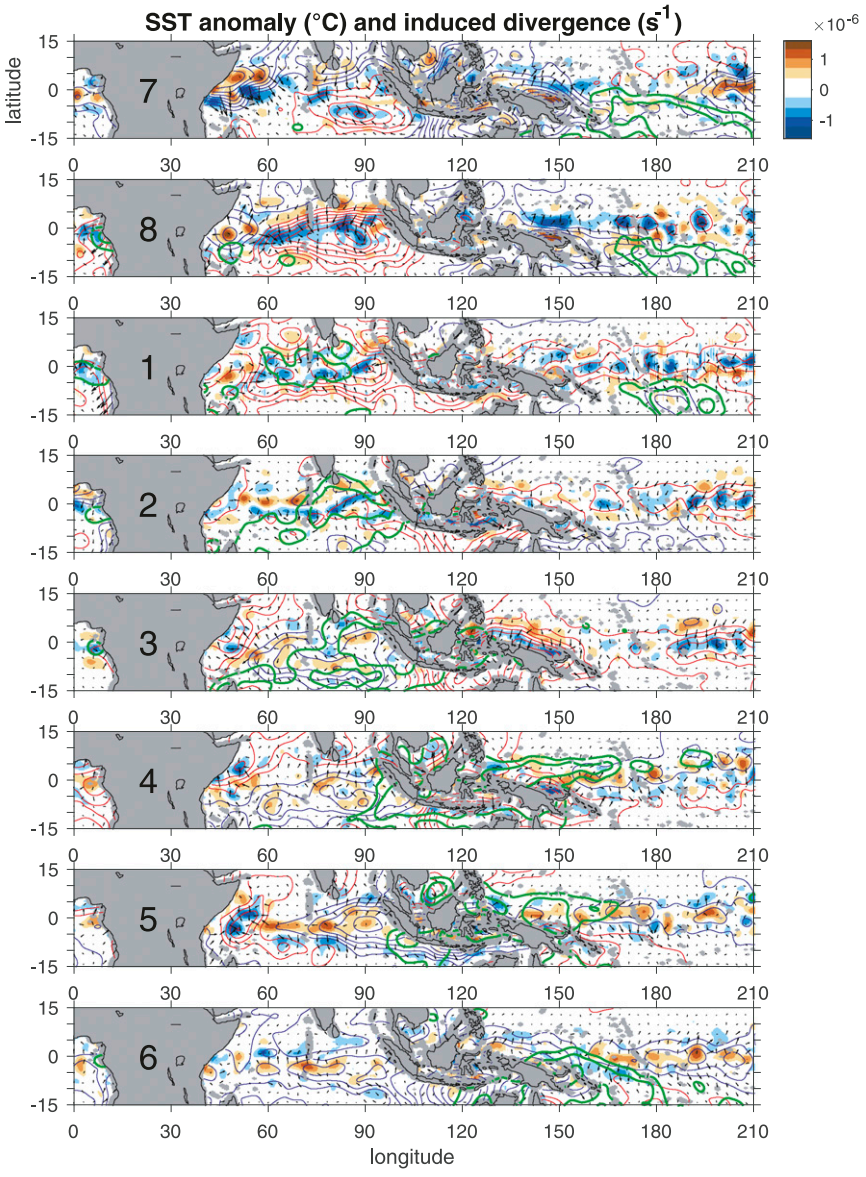

FIG. 3. TMI SST composite anomalies as in Fig. 1 and modeled ML (1010–925 hPa) mean divergence for each (numbered) phase of the RMM index. Only statistically significant divergence is shaded, i.e., exceeding about $3 \times 10^{-7}\,\mathrm{s}^{-1}$, depending on the background variance. Positive TMI precipitation anomalies are contoured in units of standard deviations (green). Vectors show the intraseasonal SST-induced wind anomaly. The guide vector over Africa is $0.2\,\mathrm{m\,s}^{-1}$.

how much moisture is exported from the atmospheric column by the compensating divergence, we divide the atmosphere vertically at $p_T = 925\,\mathrm{hPa}$. The integrated SST-induced divergence D_{ML} in the ML below p_T is compensated by opposite divergence D_A above p_T. Divergence aloft is distributed over a much deeper layer, such that

$$D_A = -(p_S - p_T)/(p_T - p_{\mathrm{tropopause}})D_{\mathrm{ML}} \approx -0.1D_{\mathrm{ML}}, \tag{15}$$

with $p_{\mathrm{tropopause}} = 200\,\mathrm{hPa}$.

The mean velocity and divergence calculated for the 925–1010-hPa ML multiplied by the ML-average moisture Q_{ML} gives the horizontal moisture convergence. From Clausius–Clapeyron and (moist) adiabatic expansion, the saturation specific humidity decreases by a factor of e^{-1} over about 250 hPa. Using this scale, the mean humidity aloft $Q_A \approx 7 \times 10^{-3}\,Q_{\mathrm{ML}}$ and the moisture export aloft $Q_A D_A \approx -7 \times 10^{-4}$; $Q_{\mathrm{ML}}D_{\mathrm{ML}}$ is much smaller than the moisture import in the ML $Q_{\mathrm{ML}}D_{\mathrm{ML}}$. A similar scaling applies to the advection term.

If the ML convergence is returned in shallower circulations, the compensating effect will be stronger because of the stronger divergence and higher humidity in the return circulation. Even if all the ML mass convergence is balanced by divergence below the freezing level (600 hPa), the compensating midlevel moisture divergence above the ML is only $Q_{\rm mid}D_{\rm mid} = -0.12\,Q_{\rm ML}D_{\rm ML}$, relatively small compared to the ML moisture convergence. The contribution of the free troposphere aloft to the moisture divergence is henceforth neglected.

The column integral moisture source in (14) is then approximated as the contributions from the ML:

$$-g^{-1}\int_{p_S}^{0} q_t\,dp = g^{-1}\int_{p_S}^{p_T}[q(\nabla_H\cdot\mathbf{V}) + \mathbf{V}\cdot\nabla_H q]\,dp. \quad (16)$$

We calculate the terms on the right-hand side from the SST-induced horizontal velocity $\mathbf{V}$ [Eqs. (7) and (8)] and divergence $\nabla_H\cdot\mathbf{V}$ [Eq. (9)], and the 925–1000-hPa November–April record mean humidity q from European Centre for Medium-Range Weather Forecasts (ECMWF) interim reanalysis (ERA-Interim; Dee et al. 2011), assuming the intraseasonal variations of q are small (Wolding et al. 2016). Using a constant mean specific humidity in every phase, the moisture convergence is a linear function of SST.

Figure 4 shows the integrated ML moisture convergence as (dynamic) latent heat flux. The horizontal advection of q is 10^{-2} times smaller than the divergence term $q(\nabla_H\cdot\mathbf{V})$, so the moisture source (Fig. 3) scales with the convergence, and we henceforth refer to the right side of (16) as the *ML moisture convergence*. The ML moisture convergence is coherent with RMM SST and convective anomalies over the Indian Ocean and the Pacific Ocean west of 150°E. The ML moisture convergence is positive over warm SST anomalies, especially in the central and eastern Indian Ocean in RMM phase 8. The moisture convergence is negative over cool SST anomalies in the eastern Indian Ocean in phase 5. The onset of convection in the central Indian Ocean is in phase 1, where there is still mean but patchy large-scale convergence.

MJO convection anomalies are weak over the central and eastern Pacific Ocean. Positive equatorial SST anomalies east of the date line in RMM phases 1–3 and negative SST in phases 5–7 may be due to the equatorial ocean response to zonal wind anomalies associated with intraseasonal convection over the western Pacific. In November–April, precipitation anomalies shift meridionally between the equator and the South Pacific convergence zone (SPCZ). These patterns project onto the RMM composite but may only be coincidentally related to the MJO.

The average ML MSE convergence for the equatorial Indian Ocean (5°N–5°S, 50°–95°E) is shown in Fig. 5. The Indian Ocean average MSE convergence has a standard deviation of 4.3 W m^{-2}, with a peak of 7.1 W m^{-2} in RMM phase 8, resulting in 39×10^{12} W integrated over the averaging area. The MSE source is positive for phases 7, 8, 1, and 2 and averages to 4.0 W m^{-2} over these four phases. This estimate of the moisture convergence is comparable to the maximum MSE tendency in advance of the MJO convective onset (Kiranmayi and Maloney 2011, their Fig. 5).

Indian Ocean average SST anomalies are positively skewed, with positive SST anomalies of 0.2°C, and negative anomalies of less than 0.1°C, yet the moisture convergence induced by the SST gradients is fairly symmetrical. The ML moisture convergence is stronger in the eastern half of the equatorial Indian Ocean, reaching ±10 W m^{-2} (root-mean-square of 7 W m^{-2}) over 72.5°–95°E. In the western Indian Ocean (50°–72.5°E) the extrema were only -3 and $+4$ W m^{-2}.

7. Summary

We compare the rate of increase of column MSE from the intraseasonal SST-induced moisture convergence with the enhanced surface MSE flux due to greater sea–air temperature and humidity differences and wind speed. Warmer SST before the convective phase of the MJO increases the sea–air temperature difference and increases the surface turbulent latent heat flux by 2–3 W m^{-2} 10 days before the maximum in precipitation (DeMott et al. 2016). The moistening due to convergence found here is in phase with the SST-driven flux anomaly and 2–3 times larger. Combining the two processes, SST contributes $\sim$10 W m^{-2} to the intraseasonal atmospheric MSE budget, bolstering the MSE source when intraseasonal wind anomalies and surface fluxes are weak in the phase of suppressed intraseasonal convection.

The SST-induced wind anomalies slightly reduce intraseasonal wind speed anomalies, but contribute only minimally to surface heat flux anomalies. The maximum SST-induced anomalous wind is westerly $\sim$0.2 m s^{-1} in the western Indian Ocean in RMM phase 8. This is against the prevailing RMM phase 8 easterly wind anomaly of 4 m s^{-1} (Wheeler and Hendon 2004, Fig. 8 therein), so it reduces of the wind speed and the turbulent surface flux anomaly by about 5%.

Johnson et al. (2015) calculate the moisture and temperature advection from the DYNAMO sounding array. Sobel et al. (2014, their Fig. 6) show that the integrated horizontal MSE advection is -2 W m^{-2} below cloud base ($p_T = 925$ hPa), while the vertical advection increases the MSE of the layer from the surface to 600–700 hPa before and during the peak in convection. Vertically integrating

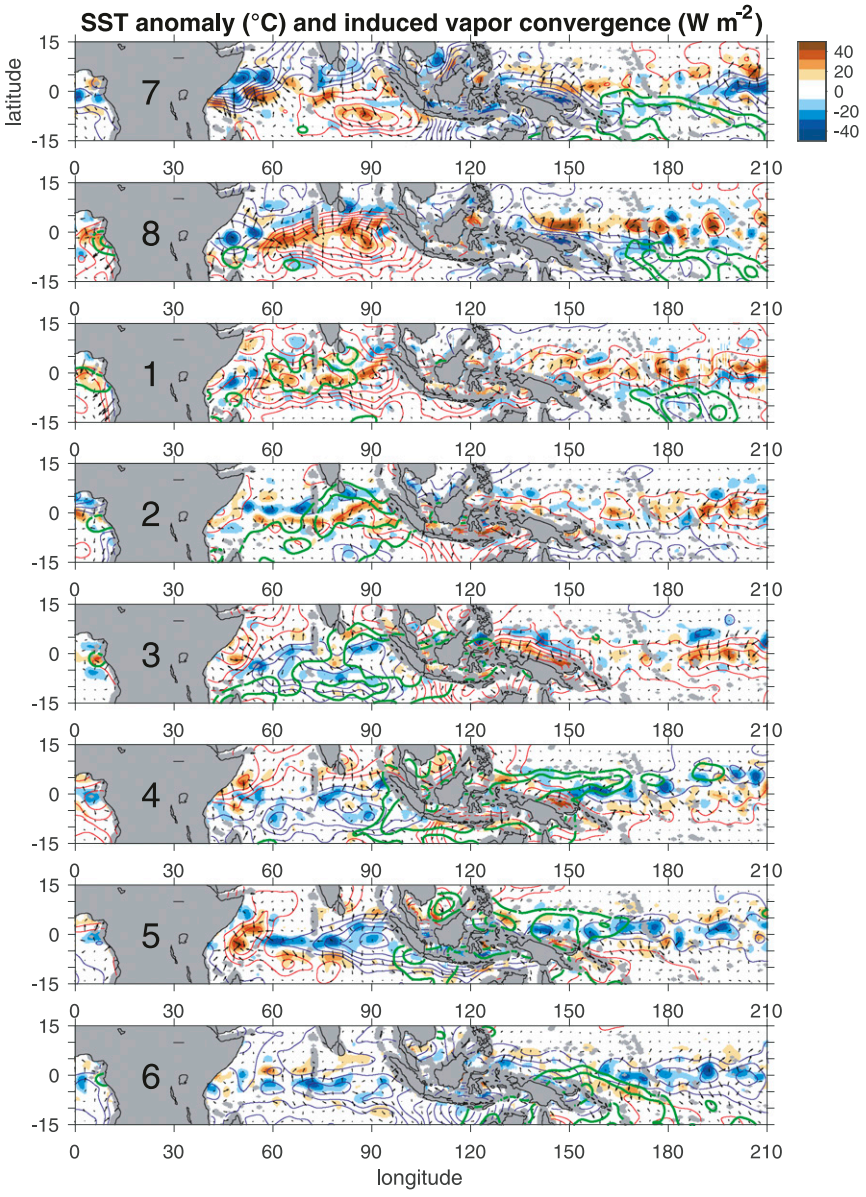

FIG. 4. As in Figs. 1 and 3, but ML-integrated moisture convergence is shaded.

just the moisture advection (Johnson et al. 2015) for the subcloud ML (from the surface to 925 hPa), vertical advection moistens the ML by 4.7 W m^{-2}, and horizontal advection dries the ML by -6.4 W m^{-2}, for a total drying (latent) advection of -1.7 W m^{-2}. Thus the $+7$ W m^{-2} intraseasonal anomaly of SST-induced moisture convergence is strong enough to cancel the mean drying advection after the convectively suppressed phase and before the active phase, and the SST-induced -6 W m^{-2} anomaly contributes to mean drying when SST is cool after the convectively active phase. Thus SST-induced moisture convergence in the ML recharges and discharges atmospheric MSE anomalies in quadrature with precipitation and in phase with intraseasonal variations of MSE over the tropical Indian and western Pacific Oceans. The intraseasonal SST-induced convergence supports moisture modes of intraseasonal convective variability. The simple diagnostic of MSE convergence over SST anomalies developed here may be evaluated for coupled models used for intraseasonal prediction of tropical convection.

Acknowledgments. The authors thank Charlotte DeMott and Larry O'Neill for early discussions that

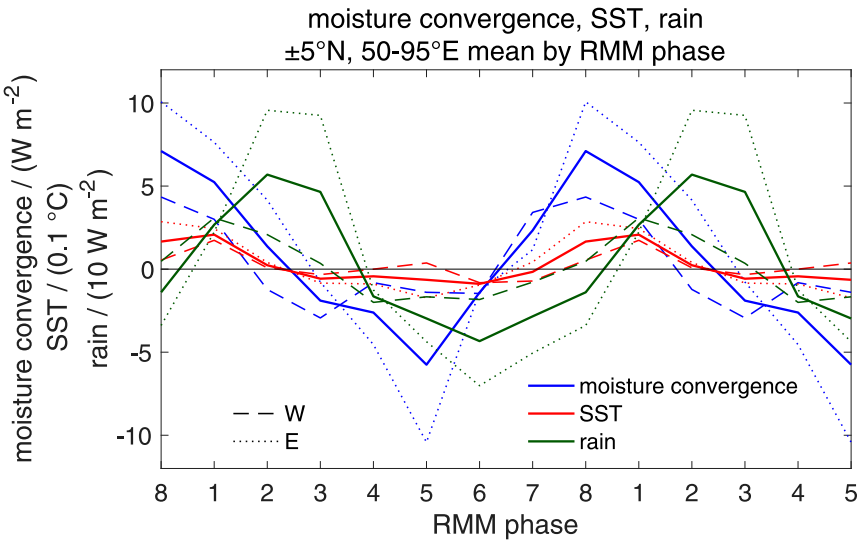

FIG. 5. Equatorial (±5°N) average SST (red), convergence (blue), and rain (green) for the Indian Ocean (50°–95°E; solid), and for the western (50°–72.5°E; dashed) and eastern (72.5°–95°E; dotted) halves of the region.

motivated this work. The gridded TRMM Microwave Imager data were produced by Remote Sensing Systems and sponsored by the NASA Earth Sciences Program. Data are available at www.remss.com/missions/tmi. The daily RMM index is available from the Australian Bureau of Meteorology, http://www.bom.gov.au/climate/mjo/. We acknowledge support from U.S. NOAA Climate Variability and Predictability projects NA18OAR4310299 and NA15OAR4310240 and Office of Naval Research projects N00014-16-1-3087 and N00014-16-1-3094. This research was supported in part by a visit to the International Centre for Theoretical Sciences (ICTS) for participation in the ''Air–Sea Interactions in the Bay of Bengal From Monsoons to Mixing'' program (Code: ICTS/ommbob2019/02).

APPENDIX

Analytical Wind and Divergence Solutions

Taking the curl and divergence of the momentum tendencies [(4) and (5)] gives equations for the curl $\phi = v_x - u_y$ and divergence $\psi = u_x + v_y$:

$$\phi_t = -r\phi + f\psi + \beta v, \tag{A1}$$

$$\psi_t = -r\psi - f\phi - \beta u - \nabla_H^2 Z. \tag{A2}$$

Near the equator f vanishes, but meridional derivative of planetary rotation, $\beta = f_y$, multiplied by the undifferentiated velocities remains, yielding the Sverdrup (1947) generalized geostrophic balance. The steady solution for the divergence is

$$\psi = [-r\nabla^2 Z - \beta(fv + ru)]/(r^2 + f^2). \tag{A3}$$

When planetary rotation is small $r \gg f$ then the divergence approaches $-(\nabla^2 Z + \beta u)/r$. For the curl,

$$\phi = [-f\nabla^2 Z + \beta(rv - fu)]/(r^2 + f^2). \tag{A4}$$

When $f \gg r$ the curl approaches $-(\nabla^2 Z + \beta u)/f$, and when $r \gg f$ it approaches $-f\nabla^2 Z/r^2 + \beta v/r$.

The eigenvalues of the time-dependent system [(4) and (5)] are $-r \pm if$. Initially rotating inertial oscillations decay exponentially to frictional balance on a time scale of r^{-1}. At 2° latitude, $f \approx 0.43\,\text{day}^{-1}$. The Rayleigh frictional damping time scale is about $r^{-1} = 0.5$ day for the $h = 780$-m subcloud mixed layer and mean ML wind of $U_0 = 6\,\text{m s}^{-1}$. At this latitude, $r > f$ and the solution decays toward frictional balance much faster than the inertial period $2\pi/f$. Thus, the SST-driven divergence approaches the steady frictionally balanced solution relatively quickly for each phase of the intraseasonal SST anomalies.

REFERENCES

Back, L. E., and C. S. Bretherton, 2006: Geographic variability in the export of moist static energy and vertical motion profiles in the tropical Pacific. *Geophys. Res. Lett.*, **33**, L17810, https://doi.org/10.1029/2006GL026672.

——, and ——, 2009: On the relationship between SST gradients, boundary layer winds, and convergence over the tropical oceans. *J. Climate*, **22**, 4182–4196, https://doi.org/10.1175/2009JCLI2392.1.

Clayson, C. A., and A. S. Bogdanoff, 2013: The effect of diurnal sea surface temperature warming on climatological air–sea fluxes.

J. Climate, **26**, 2546–2556, https://doi.org/10.1175/JCLI-D-12-00062.1.

Dee, D. P., and Coauthors, 2011: The ERA-Interim reanalysis: Configuration and performance of the data assimilation system. *Quart. J. Roy. Meteor. Soc.*, **137**, 553–597, https://doi.org/10.1002/qj.828.

Del Genio, A. D., and Y. Chen, 2015: Cloud-radiative driving of the Madden–Julian oscillation as seen by the A-Train. *J. Geophys. Res. Atmos.*, **120**, 5344–5356, https://doi.org/10.1002/2015JD023278.

DeMott, C. A., J. J. Benedict, N. P. Klingaman, S. J. Woolnough, and D. A. Randall, 2016: Diagnosing ocean feedbacks to the MJO: SST-modulated surface fluxes and the moist static energy budget. *J. Geophys. Res.*, **121**, 8350–8373. https://doi.org/10.1002/2016JD025098.

de Szoeke, S. P., J. B. Edson, J. R. Marion, C. W. Fairall, and L. Bariteau, 2015: The MJO and air–sea interaction in TOGA COARE and DYNAMO. *J. Climate*, **28**, 597–622, https://doi.org/10.1175/JCLI-D-14-00477.1.

——, E. D. Skyllingstad, P. Zuidema, and A. S. Chandra, 2017: Cold pools and their influence on the tropical marine boundary layer. *J. Atmos. Sci.*, **74**, 1149–1168, https://doi.org/10.1175/JAS-D-16-0264.1.

Emanuel, K. A., 1987: An air–sea interaction model of intraseasonal oscillations in the tropics. *J. Atmos. Sci.*, **44**, 2324–2340, https://doi.org/10.1175/1520-0469(1987)044<2324:AASIMO>2.0.CO;2.

Flatau, M., P. J. Flatau, P. Phoebus, and P. P. Niiler, 1997: The feedback between equatorial convection and local radiative and evaporative processes: The implications for intraseasonal oscillations. *J. Atmos. Sci.*, **54**, 2373–2386, https://doi.org/10.1175/1520-0469(1997)054<2373:TFBECA>2.0.CO;2.

Gentemann, C. L., C. J. Donlon, A. Stuart-Menteth, and F. J. Wentz, 2003: Diurnal signals in satellite sea surface temperature measurements. *Geophys. Res. Lett.*, **30**, 1140, https://doi.org/10.1029/2002GL016291.

——, F. J. Wentz, C. A. Mears, and D. K. Smith, 2004: In situ validation of Tropical Rainfall Measuring Mission microwave sea surface temperatures. *J. Geophys. Res. Oceans*, **109**, C04021, https://doi.org/10.1029/2003JC002092.

Gottschalck, J., and Coauthors, 2010: A framework for assessing operational Madden–Julian oscillation forecasts. *Bull. Amer. Meteor. Soc.*, **91**, 1247–1258, https://doi.org/10.1175/2010BAMS2816.1.

Hendon, H. H., and J. Glick, 1997: Intraseasonal air–sea interaction in the tropical Indian and Pacific Oceans. *J. Climate*, **10**, 647–661, https://doi.org/10.1175/1520-0442(1997)010<0647:IASIIT>2.0.CO;2.

Hsu, P.-C., and T. Li, 2012: Role of the boundary layer moisture asymmetry in causing the eastward propagation of the Madden-Julian oscillation. *J. Climate*, **25**, 4914–4931, https://doi.org/10.1175/JCLI-D-11-00310.1.

Johnson, R. H., and P. E. Ciesielski, 2013: Structure and properties of Madden–Julian oscillations deduced from DYNAMO sounding arrays. *J. Atmos. Sci.*, **70**, 3157–3179, https://doi.org/10.1175/JAS-D-13-065.1.

——, ——, J. H. Ruppert, and M. Katsumata, 2015: Sounding-based thermodynamic budgets for DYNAMO. *J. Atmos. Sci.*, **72**, 598–622, https://doi.org/10.1175/JAS-D-14-0202.1.

Kang, I.-S., and H.-M. Kim, 2010: Assessment of MJO predictability for boreal winter with various statistical and dynamical models. *J. Climate*, **23**, 2368–2378, https://doi.org/10.1175/2010JCLI3288.1.

Kessler, W. S., 2001: EOF representations of the Madden–Julian oscillation and its connection with ENSO. *J. Climate*, **14**, 3055–3061, https://doi.org/10.1175/1520-0442(2001)014<3055:EROTMJ>2.0.CO;2.

Kiladis, G. N., K. H. Straub, and P. T. Haertel, 2005: Zonal and vertical structure of the Madden–Julian oscillation. *J. Atmos. Sci.*, **62**, 2790–2809, https://doi.org/10.1175/JAS3520.1.

Kiranmayi, L., and E. D. Maloney, 2011: Intraseasonal moist static energy budget in reanalysis data. *J. Geophys. Res.*, **116**, D21117, https://doi.org/10.1029/2011JD016031.

Krishnamurti, T. N., D. K. Oosterhof, and A. V. Mehta, 1988: Air–sea interaction on the time scale of 30 to 50 days. *J. Atmos. Sci.*, **45**, 1304–1322, https://doi.org/10.1175/1520-0469(1988)045<1304:AIOTTS>2.0.CO;2.

Lim, Y., S.-W. Son, and D. Kim, 2018: MJO prediction skill of the subseasonal-to-seasonal prediction models. *J. Climate*, **31**, 4075–4094, https://doi.org/10.1175/JCLI-D-17-0545.1.

Lindzen, R. S., and S. Nigam, 1987: On the role of sea surface temperature gradients in forcing low-level winds and convergence in the tropics. *J. Atmos. Sci.*, **44**, 2418–2436, https://doi.org/10.1175/1520-0469(1987)044<2418:OTROSS>2.0.CO;2.

Madden, R. A., and P. R. Julian, 1971: Detection of a 40–50 day oscillation in the zonal wind in the tropical Pacific. *J. Atmos. Sci.*, **28**, 702–708, https://doi.org/10.1175/1520-0469(1971)028<0702:DOADOI>2.0.CO;2.

Maloney, E. D., and A. H. Sobel, 2004: Surface fluxes and ocean coupling in the tropical intraseasonal oscillation. *J. Climate*, **17**, 4368–4386, https://doi.org/10.1175/JCLI-3212.1.

Marshall, A. G., O. Alves, and H. H. Hendon, 2008: An enhanced moisture convergence–evaporation feedback mechanism for MJO air–sea interaction. *J. Atmos. Sci.*, **65**, 970–986, https://doi.org/10.1175/2007JAS2313.1.

Matthews, A. J., 2008: Primary and successive events in the Madden–Julian oscillation. *Quart. J. Roy. Meteor. Soc.*, **134**, 439–453, https://doi.org/10.1002/qj.224.

Moteki, Q., 2015: Equatorially antisymmetric features in the initiation processes of the Madden–Julian oscillation observed in late October during CINDY2011. *J. Meteor. Soc. Japan*, **93A**, 59–79, https://doi.org/10.2151/JMSJ.2015-040.

Moum, J. N., and Coauthors, 2014: Air–sea interactions from westerly wind bursts during the November 2011 MJO in the Indian Ocean. *Bull. Amer. Meteor. Soc.*, **95**, 1185–1199, https://doi.org/10.1175/BAMS-D-12-00225.1.

Neelin, J. D., I. M. Held, and K. H. Cook, 1987: Evaporation–wind feedback and low-frequency variability in the tropical atmosphere. *J. Atmos. Sci.*, **44**, 2341–2348, https://doi.org/10.1175/1520-0469(1987)044<2341:EWFALF>2.0.CO;2.

Pujiana, K., J. N. Moum, and W. D. Smyth, 2017: The role of turbulence in redistributing upper ocean heat, freshwater, and momentum in response to the MJO in the equatorial Indian Ocean. *J. Phys. Oceanogr.*, **48**, 197–220, https://doi.org/10.1175/JPO-D-17-0146.1

Raymond, D. J., and Ž. Fuchs, 2009: Moisture modes and the Madden–Julian oscillation. *J. Climate*, **22**, 3031–3046, https://doi.org/10.1175/2008JCLI2739.1.

Rydbeck, A. V., and T. G. Jensen, 2017: Oceanic impetus for convective onset of the Madden–Julian oscillation in the western Indian Ocean. *J. Climate*, **30**, 4299–4316, https://doi.org/10.1175/JCLI-D-16-0595.1.

Shinoda, T., H. H. Hendon, and J. Glick, 1998: Intraseasonal variability of surface fluxes and sea surface temperature in the tropical western Pacific and Indian Oceans. *J. Climate*, **11**, 1685–1702, https://doi.org/10.1175/1520-0442(1998)011<1685:IVOSFA>2.0.CO;2.

Sobel, A. H., J. Nilsson, and L. M. Polvani, 2001: The weak temperature gradient approximation and balanced tropical moisture waves. *J. Atmos. Sci.*, **58**, 3650–3665, https://doi.org/10.1175/1520-0469(2001)058<3650:TWTGAA>2.0.CO;2.

——, S. Wang, and D. Kim, 2014: Moist static energy budget of the MJO during DYNAMO. *J. Atmos. Sci.*, **71**, 4276–4291, https://doi.org/10.1175/JAS-D-14-0052.1.

Stan, C., 2018: The role of SST variability in the simulation of the MJO. *Climate Dyn.*, **51**, 2943–2964, https://doi.org/10.1007/S00382-017-4058-2.

Stevens, B., J. Duan, J. C. McWilliams, M. Münnich, and J. D. Neelin, 2002: Entrainment, Rayleigh friction, and boundary layer winds over the tropical Pacific. *J. Climate*, **15**, 30–44, https://doi.org/10.1175/1520-0442(2002)015<0030:ERFABL>2.0.CO;2.

Straub, K. H., 2013: MJO initiation in the Real-Time Multivariate MJO Index. *J. Climate*, **26**, 1130–1151, https://doi.org/10.1175/JCLI-D-12-00074.1.

Sverdrup, H. U., 1947: Wind-driven currents in a baroclinic ocean; with application to the equatorial currents of the eastern Pacific. *Proc. Natl. Acad. Sci. USA*, **33**, 318–326, https://doi.org/10.1073/pnas.33.11.318.

Wang, B., and T. Li, 1994: Convective interaction with boundary-layer dynamics in the development of a tropical intraseasonal system. *J. Atmos. Sci.*, **51**, 1386–1400, https://doi.org/10.1175/1520-0469(1994)051<1386:CIWBLD>2.0.CO;2.

——, F. Liu, and G. Chen, 2016: A trio-interaction theory for Madden–Julian oscillation. *Geosci. Lett.*, **3**, 34, https://doi.org/10.1186/s40562-016-0066-z.

Wang, W., M.-P. Hung, S. J. Weaver, A. Kumar, and X. Fu, 2014: MJO prediction in the NCEP Climate Forecast System version 2. *Climate Dyn.*, **42**, 2509–2520, https://doi.org/10.1007/s00382-013-1806-9.

Wentz, F. J., C. L. Gentemann, and K. A. Hilburn, 2015: Remote Sensing Systems TRMM TMI Daily Environmental Suite on 0.25 deg grid, Version 7.1. Remote Sensing Systems, accessed March 2015, www.remss.com/missions/tmi.

Wheeler, M. C., and H. H. Hendon, 2004: An all-season real-time multivariate MJO index: Development of an index for monitoring and prediction. *Mon. Wea. Rev.*, **132**, 1917–1932, https://doi.org/10.1175/1520-0493(2004)132<1917:AARMMI>2.0.CO;2.

Wolding, B. O., E. D. Maloney, and M. Branson, 2016: Vertically resolved weak temperature gradient analysis of the Madden-Julian oscillation in SP-CESM. *J. Adv. Model. Earth Syst.*, **8**, 1586–1619, https://doi.org/10.1002/2016MS000724.

Woolnough, S. J., J. M. Slingo, and B. J. Hoskins, 2000: The relationship between convection and sea surface temperature on intraseasonal timescales. *J. Climate*, **13**, 2086–2104, https://doi.org/10.1175/1520-0442(2000)013<2086:TRBCAS>2.0.CO;2.

Yoneyama, K., C. Zhang, and C. N. Long, 2013: Tracking pulses of the Madden–Julian oscillation. *Bull. Amer. Meteor. Soc.*, **94**, 1871–1891, https://doi.org/10.1175/BAMS-D-12-00157.1.

Zhang, G. J., and M. J. McPhaden, 1995: The relationship between sea surface temperature and latent heat flux in the equatorial Pacific. *J. Climate*, **8**, 589–605, https://doi.org/10.1175/1520-0442(1995)008<0589:TRBSST>2.0.CO;2.